

# Thermodynamic evidence for polaron stabilization inside the antiferromagnetic order of $\text{Eu}_5\text{In}_2\text{Sb}_6$

H. Dawczak-Dębicki,<sup>1</sup> M. Victoria Ale Crivillero,<sup>1</sup> M. S. Cook,<sup>2</sup> S. M. Thomas,<sup>2</sup> Priscila F. S. Rosa,<sup>2</sup> J. Müller,<sup>3</sup> U. K. Röbler,<sup>4</sup> P. Schlottmann,<sup>5</sup> and S. Wirth<sup>1</sup>

<sup>1</sup>*Max Planck Institute for Chemical Physics of Solids, 01187 Dresden, Germany*

<sup>2</sup>*Los Alamos National Laboratory, Los Alamos, NM 87545, USA*

<sup>3</sup>*Institute of Physics, Goethe-University Frankfurt, 60438 Frankfurt (M), Germany*

<sup>4</sup>*IFW Dresden, Helmholtzstraße 20, 01069 Dresden, Germany*

<sup>5</sup>*Department of Physics, Florida State University, Tallahassee, Florida 32306, USA*

(Dated: November 18, 2024)

Materials exhibiting electronic inhomogeneities at the nanometer scale have enormous potential for applications. Magnetic polarons are one such type of inhomogeneity which link the electronic, magnetic and lattice degrees of freedom in correlated matter and often give rise to colossal magnetoresistance. Here, we investigate single crystals of  $\text{Eu}_5\text{In}_2\text{Sb}_6$  by thermal expansion and magnetostriction along different crystallographic directions. These data provide compelling evidence for the formation of magnetic polarons in  $\text{Eu}_5\text{In}_2\text{Sb}_6$  well above the magnetic ordering temperature. More specifically, our results are consistent with anisotropic polarons with varying extent along the different crystallographic directions. A crossover revealed within the magnetically ordered phase can be associated with a surprising stabilization of ferromagnetic polarons within the global antiferromagnetic order upon decreasing temperature. These findings make  $\text{Eu}_5\text{In}_2\text{Sb}_6$  a rare example of such coexisting and competing magnetic orders and, importantly, shed new light on colossal magnetoresistive behavior beyond manganites.

## Introduction

Materials in which the electrical and magnetic properties are intertwined are of considerable interest from a fundamental point of view as well as for applications, specifically in spintronics [1, 2]. Here, correlated materials are of particular significance because of their often inherent coupling of lattice, charge, orbital and/or spin degrees of freedom. As a consequence of these multiple interactions electronically inhomogeneous states can arise [3]. Moreover, these multiple interactions may give rise to large responses upon small perturbations, a desired scenario for possible applications. Prime examples of electronically correlated, spatially inhomogeneous materials are the cuprate superconductors with high transition temperatures [4, 5] or manganites exhibiting colossal magnetoresistance (CMR) effects [6].

Eu-based compounds are often prone to coupled charge and spin degrees of freedom: A strong exchange interac-

tion between charge carriers and the localized spin of the  $\text{Eu}^{2+}$  ions [7, 8] may result in a localization of these charge carriers at  $\text{Eu}^{2+}$  sites. The resulting quasiparticle made up of the localized charge carriers and the Eu moment is referred to as a magnetic polaron [9, 10] and exemplifies the interplay between electrical and magnetic properties, the hallmark of spintronics [11, 12]. A prerequisite for polaron formation is a low enough carrier concentration, which assures polarons remain localized and do not populate the materials volume. In this respect, Zintl phases [13] emerge as a promising playground. In particular,  $\text{Eu}_5\text{In}_2\text{Sb}_6$  has been recently reported [14–16] as a narrow-gap semiconductor [17, 18] whose properties are consistent with polaron formation. Notably, this material is a magnetic counterpart to  $\text{Ba}_5\text{In}_2\text{Sb}_6$  [19], which crystallizes in the non-symmorphic space group *Pbma* (No. 55) and has been predicted to display topological surface states [20, 21]. Hence,  $\text{Eu}_5\text{In}_2\text{Sb}_6$  may combine topologically nontrivial surface states with magnetism and polaron formation, albeit only the latter two properties have been experimentally established so far [14–16]. Also, a remarkably large negative magnetoresistance, comparable to the best CMR manganites, was observed in  $\text{Eu}_5\text{In}_2\text{Sb}_6$  [14, 16]. The price to be paid for this potentially interesting combination of properties is the complex orthorhombic structure of  $\text{Eu}_5\text{In}_2\text{Sb}_6$  with three crystallographically different Eu sites [17], resulting in a complicated magnetic phase diagram with at least two antiferromagnetic phases ( $T_{N1} \approx 14.1$  K,  $T_{N2} \approx 7.2$  K) and entangled magnetization processes [14, 15, 22, 23]. It must also be pointed out that despite an orbital angular momentum of  $L = 0$  of the  $\text{Eu}^{2+}$  ions in this compound, strong anisotropies of the transport properties and the magnetic susceptibility in the magnetically ordered phase have been observed indicating competing magnetic interactions. In particular, the low symmetry of the Eu sublattices allows for the existence of Dzyaloshinskii-Moriya interactions and spin canting [15]. Thus, the magnetic structure of  $\text{Eu}_5\text{In}_2\text{Sb}_6$  is highly complex [15, 22, 23] and not yet fully resolved in all detail.

In an effort to shed light on the intriguing properties of  $\text{Eu}_5\text{In}_2\text{Sb}_6$  we conducted thermal expansion and magnetostriction measurements along the different

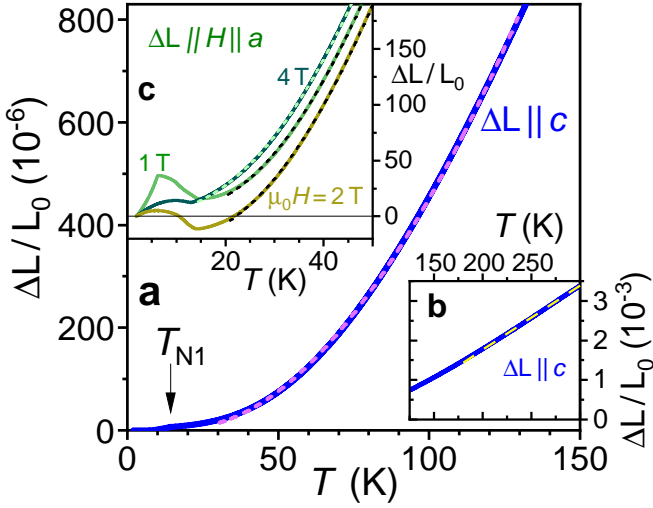


**Fig. 1. Fits of thermal expansion data.** **a**  $\Delta L(T)/L_0$  can very well be fitted to a model containing electronic and phononic contributions [24] for  $35 \text{ K} \lesssim T \lesssim 130 \text{ K}$  and **b** is linear in  $T$  above 175 K, respectively. **c**: Fits to the model [24] for  $\Delta L(T, H)/L_0$  measured along the  $a$  axis and at selected fields (same data as in Fig. 4a, units of  $10^{-6}$ ). All dashed lines are fit results.

crystallographic directions of single crystals. The results provide further evidence for the formation of non-spherical polarons far above the Néel temperature  $T_N$ . These polarons give rise to an extraordinarily rich and anisotropic magnetoresistive behavior. Within the antiferromagnetically ordered phase, our results are in excellent agreement with the established phase diagrams. Additionally, however, these dilatation data reveal a crossover which is associated with the coexistence of ferromagnetic (fm) polarons and antiferromagnetic (afm) long-range order. Surprisingly, these polarons become more stable upon lowering the temperature. This crossover could not be traced by any other, i.e. magnetic, transport or specific heat measurement, a fact that points to magnetoelastic coupling effects as its origin and that underscores the remarkable sensitivity of expansion measurements, establishing them as pivotal tool to unveil subtle phenomena.

## Results

### Paramagnetic regime

We start off by considering the paramagnetic regime before discussing the magnetically much more complex afm low-temperature regime. Thermal expansion data up to room temperature for measurements along the  $c$  axis are presented in Fig. 1. For  $T \gtrsim 175 \text{ K}$ , the relative length change  $\Delta L(T)/L_0$  increases linearly with  $T$  within experimental resolution (Fig. 1b), as expected for a material with a Debye temperature  $\theta_D \approx 197 \text{ K}$  [16]. Here,  $L_0$  is the sample length at a reference temperature. Between  $35 \text{ K} \lesssim T \lesssim 130 \text{ K}$ , Fig. 1a,  $\Delta L(T)/L_0$  can be well

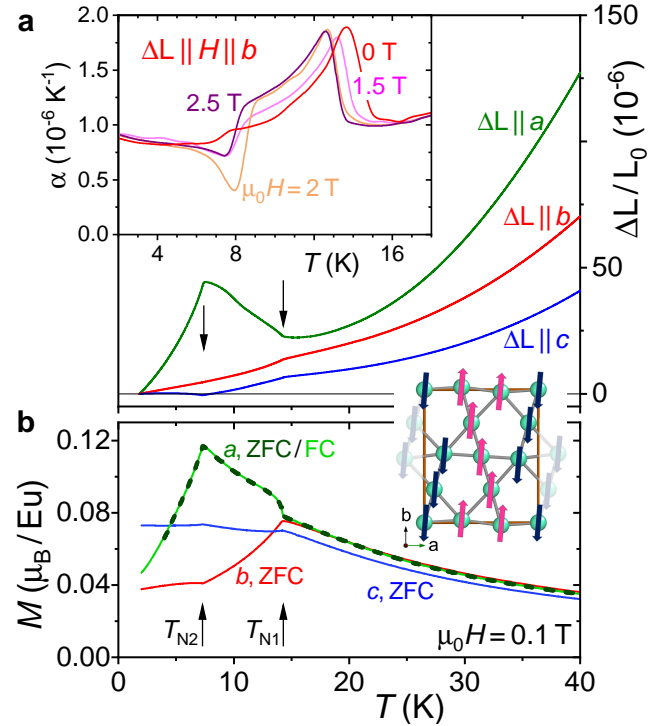


**Fig. 2. Comparison of thermal expansion and magnetization.** **a** Relative length change  $\Delta L(T)/L_0$  measured along the three main crystallographic directions of  $\text{Eu}_5\text{In}_2\text{Sb}_6$ . Inset: Low-temperature thermal expansion coefficient  $\alpha(T, H)$  along the  $b$  axis and for representative magnetic fields  $\mu_0 H = 0, 1.5, 2.0, 2.5 \text{ T}$ . The feature near 8 K evolves non-monotonically with  $H$ . **b** Zero-field cooled (ZFC) magnetization of  $\text{Eu}_5\text{In}_2\text{Sb}_6$  measured in  $\mu_0 H = 0.1 \text{ T}$  for the three directions. For comparison, the field-cooled (FC) curve along the  $a$  axis is also shown. Arrows mark  $T_{N1}$  and  $T_{N2}$ , respectively. Sketch: spin configuration just below  $T_{N1}$  in phase I, as suggested in [15].

described by a model in which electronic and phononic contributions are considered [24, 25], see Supplementary Note 2 and Supplementary Table I. For simplicity, we relied on our specific heat results [16] and conducted the fits with  $\theta_D = 197 \text{ K}$  and without Einstein modes. For measurements along the  $a$  axis, the fits hold down to about 25 K, and with an applied field of 4 T even to slightly lower  $T$ , cf. Fig. 1c. We note that using different fitting procedures does not change our findings qualitatively (see Supplementary Figures 2 and 3).

Since thermodynamic, magnetic and electronic transport properties of  $\text{Eu}_5\text{In}_2\text{Sb}_6$  all indicate a clear impact of magnetic polarons below 40 – 50 K [14, 16, 26, 27], the deviations of  $\Delta L(T)/L_0$  from the modelled  $T$ -behavior can safely be associated with such polarons. In  $\text{Eu}_5\text{In}_2\text{Sb}_6$ , these nanoscale clusters are likely anisotropic in shape with the shortest direction along  $c$  and fm alignment of the  $\text{Eu}^{2+}$  moments within the polaron in the  $ab$  plane [15, 26, 27]. It is well established that magnetic polarons can induce lattice distortions [28–30]. In Fig. 2a, we fo-

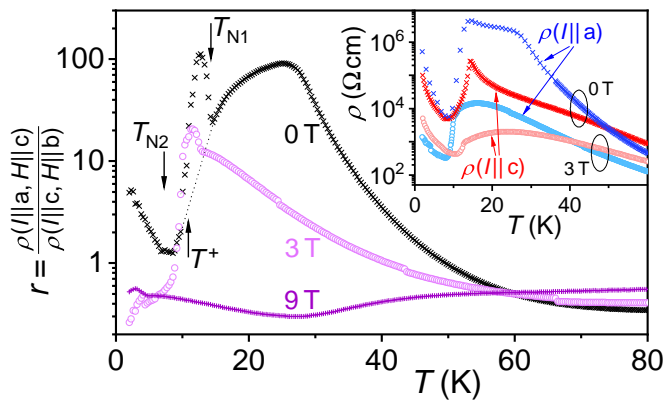


**Fig. 3. Analysis of resistivities.** Ratio  $r$  of resistivities  $\rho$  measured along  $I \parallel a$ ,  $\mathbf{H} \parallel c$  versus  $I \parallel c$ ,  $\mathbf{H} \parallel b$  for fields  $\mu_0 H = 0$  T ( $\times$ ), 3 T ( $\circ$ ) and 9 T ( $+$ ). The dotted line is a guide to the eye. Inset: individual  $\rho$  values;  $I \parallel a$  bluish,  $I \parallel c$  reddish for 0 T ( $\times$ ) and 3 T ( $\circ$ ).  $T^+$  marks the crossover into an inhomogeneous, polaronic state upon lowering  $T$ , here shown for  $H = 0$ .

cus on  $T \leq 40$  K and present the relative length changes  $\Delta L(T)/L_0$  as measured along the three main crystallographic directions of  $\text{Eu}_5\text{In}_2\text{Sb}_6$ . Clearly, there are large anisotropies observed, as already seen in magnetic, transport and piezoresistive measurements [14, 16, 26] and treated by density functional theory calculation [15]. For all directions, however, a kink is observed at  $\approx 14.3$  K in zero magnetic field, a temperature associated with  $T_{N1}$  [14, 16]. The transition near  $T_{N2} \approx 7.2$  K is most pronounced for  $\Delta L^{100}(T)/L_0$  along the  $a$  axis. In fact, the strong length increase with increasing  $T$  below 7.2 K and the subsequent decrease up to 14.3 K mimics very nicely the strongly  $T$ -dependent magnetization  $M(T)$  measured along the  $a$  axis, as shown in Fig. 2b. Similarly, thermal expansion and magnetization exhibit the smallest change with temperature for measurements along the  $c$  axis. Here we emphasize again that  $L = 0$  for  $\text{Eu}^{2+}$  and hence, crystalline electric field (CEF) effects are negligible to first order. This implies that magnetic interactions not only determine the anisotropic magnetization behavior in  $\text{Eu}_5\text{In}_2\text{Sb}_6$  but also its thermal expansion in magnetic fields and magnetostrictive behavior [25, 31].

We now attempt to interpret the resistive behavior of  $\text{Eu}_5\text{In}_2\text{Sb}_6$ , Fig. 3. In order to minimize dependencies on specific samples on the one hand, and focus on the anisotropy of the polarons on the other hand, we consider the ratio of resistivities along different directions,  $r = \rho_{I \parallel a} / \rho_{I \parallel c}$ , where  $\rho_{I \parallel a}$  and  $\rho_{I \parallel c}$  are the resistivities measured for  $I \parallel a$  ( $\mathbf{H} \parallel c$ ) and  $I \parallel c$  ( $\mathbf{H} \parallel b$ ), respectively [16]. The infinite  $[\text{In}_2\text{Sb}_6]^{10-}$  ribbons of the  $\text{Eu}_5\text{In}_2\text{Sb}_6$  structure along  $c$  support preferred charge transport along this direction [17] upon lowering  $T$  below 50 K, and  $r(T)$  increases strongly at zero field. This increase of  $r(T)$  is intercepted below 30 K by the inter-

action of the polarons which are more extended in the  $ab$  plane. This results in a shoulder of  $\rho_{I \parallel a}$  and a pronounced maximum in  $r(T)$ . The sharp increase of  $r(T)$  below  $T = 14.4$  K reflects the onset of afm ordering at  $T_{N1}$ .

In a magnetic field of 3 T parallel to  $c$ , the polarons grow in size along  $c$  and hence, abate their anisotropy, such that the differences in  $\rho_{I \parallel a}$  and  $\rho_{I \parallel c}$  (for fields along  $c$  and  $b$ , respectively) are much less pronounced; likely the maximum in  $r(T)$  is then shifted close to  $T_{N1}$ . In the nearly field-polarized state at 9 T (saturation of magnetization is achieved near 10 T at 2 K [16]), the fm polarons have grown further, overlapped and likely merged into their surroundings. In consequence, only a weak temperature dependence of  $r(T)$  is observed.

### Antiferromagnetically ordered regime

Considering the formation of polarons well above the afm ordered phase as being established we now investigate the fate of these polarons upon cooling to below  $T_{N1}$ . The transitions at  $T_{N1}$  and  $T_{N2}$  can easily be recognized in the dilatation data along the different crystallographic directions, Fig. 2 and Fig. 4, particularly from the coefficients of thermal expansion  $\alpha(T) = (1/L_0)(dL/dT)$  and magnetostriction  $\lambda = (1/L_0)\partial L/\partial H$ . In Fig. 5 we include these results into the  $T$ - $H$  phase diagrams obtained from magnetic, specific heat and transport measurements (faint data points and lines from Ale Crivillero *et al.*[16]) for the three main crystallographic directions. In order to allow for such a comparison the

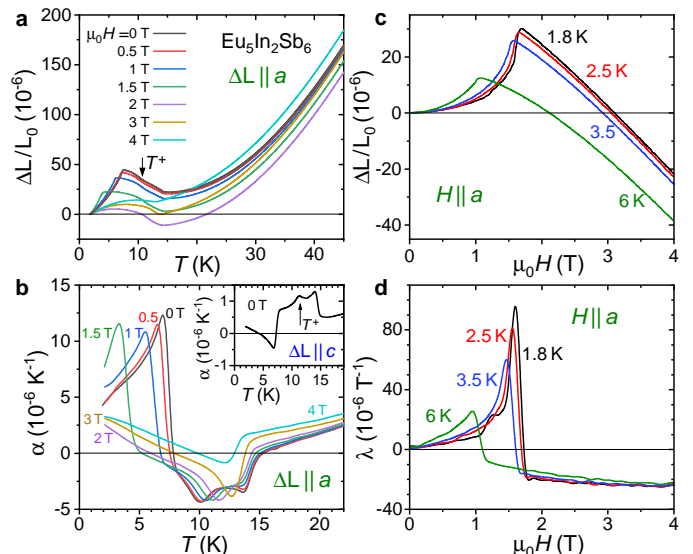


**Fig. 4. Detailed thermal expansion and magnetostriction along  $a$  axis.** **a** Length change  $\Delta L(T)/L_0$  and **b** thermal expansion coefficient  $\alpha(T)$  measured at different magnetic fields  $H$  along the  $a$  axis. Inset:  $\alpha(T, H = 0)$  along the  $c$  axis. **c** Magnetostriction  $\Delta L(H)/L_0$  and **d** magnetostriction coefficient  $\lambda$  for  $\mathbf{H} \parallel a$  at different  $T$ .

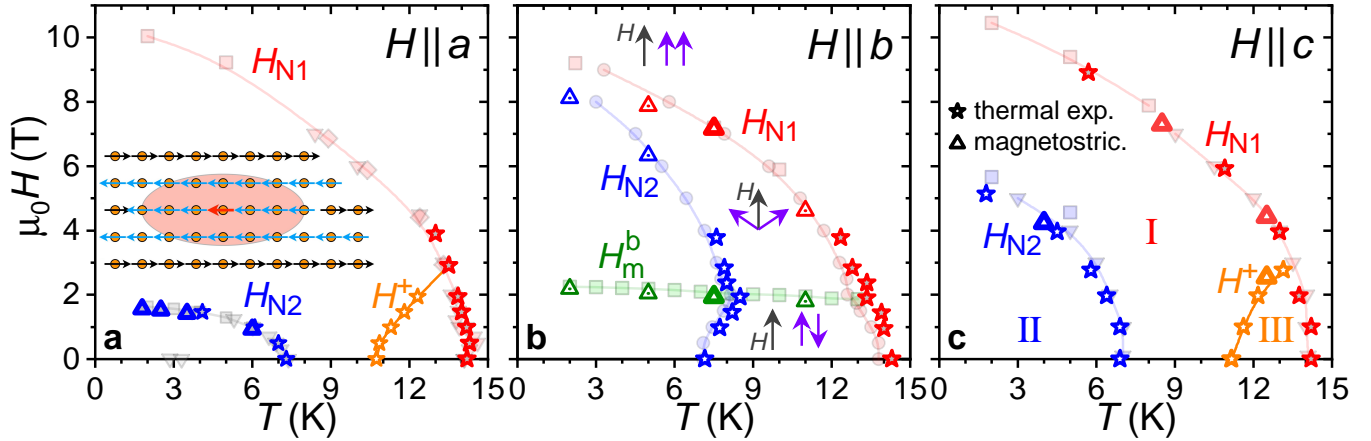


**Fig. 5.**  $H$ - $T$  phase diagrams of  $\text{Eu}_5\text{In}_2\text{Sb}_6$  for the three main crystallographic directions: **a** along  $a$  axis, **b** along  $b$  and **c** along  $c$ . The faint lines and data points, reproduced [16] for direct comparison, result from specific heat and magnetic measurements. Thermal expansion and magnetostriction results are indicated by  $\star$  and  $\Delta$ , respectively (dotted triangles for  $\mathbf{H} \parallel b$  indicate results obtained with a different setup, see Supplementary Note 4 and Supplementary Figure 5).  $H_m^b$  marks a metamagnetic behavior. The three regions I, II and III between  $H_{N1}$  and  $H_{N2}$ , below  $H_{N2}$ , and between  $H_{N1}$  and  $H^+$ , respectively, are marked in **c**. Here,  $H_{N1}$  and  $H_{N2}$  mark antiferromagnetic (afm) phase transitions while  $H^+$  signals a crossover. In **a**, an anisotropic ferromagnetic polaron at zero field is sketched within afm global order, a situation expected in region I. The polarons' shortest dimension is expected along the crystallographic  $c$  direction and the Eu moments are aligned in the  $ab$  plane.

samples' demagnetizing effects were taken into consideration.  $H_{N1}$  and  $H_{N2}$  describe the field dependencies of  $T_{N1}$  and  $T_{N2}$ , respectively. Clearly, our dilatation data trace the transitions at  $H_{N1}$  (red) and  $H_{N2}$  (blue) very well. This emphasizes again that the effects observed in thermal expansion and magnetostriction are primarily related to the magnetic structure of  $\text{Eu}_5\text{In}_2\text{Sb}_6$ . Further support for such an assignment comes from the magnetostriction measurement  $\Delta L(H)/L_0$  at  $T = 7.5$  K along the crystallographic  $b$  direction which exhibits a jump at  $\mu_0 H_m^b \approx 2$  T, red and orange data in Fig. 6b. Here,  $H_m^b$  marks the metamagnetic behavior associated with a spin flop [16] as sketched in Fig. 5b.

#### Analysis of magnetostrictive behavior

As clearly seen in  $\alpha(T, H)$  along the  $a$  and the  $c$  axis these data reveal another, field-dependent feature just below  $T_{N1}$  denoted as  $H^+$  in Fig. 5 (orange data). In the following, we inspect this feature by considering the magnetostriction for  $\mathbf{H} \parallel c$  within the three regions marked in Fig. 5c. Note that  $c$  is the magnetically hard direction and applying  $\mathbf{H} \parallel c$  rotates the local moments out of the  $ab$ -plane without spin-flop.

As shown in Fig. 6a, at  $T = 4$  K and below  $H_{N2}$ , region II, where Eu moments at all three lattice sites are ordered [22, 23], the sample contracts with increasing  $H$  in an impeccable  $H^2$ -fashion. This results from [32, 33]  $\Delta L(H) \sim -[M(H)/M_s]^2$  ( $M_s$  is the saturation magnetization) and  $M(H) \sim H$  in this regime [16]. In the same phase space, the sample contracts not only with  $H$ ,

but also with increasing  $T$ , cf. Figs. 2a and 4. This is, however, outweighed by a much larger extension along  $a$ , both with increasing  $T$  and  $H$ , such that the total sample volume increases. These effects are reversed upon

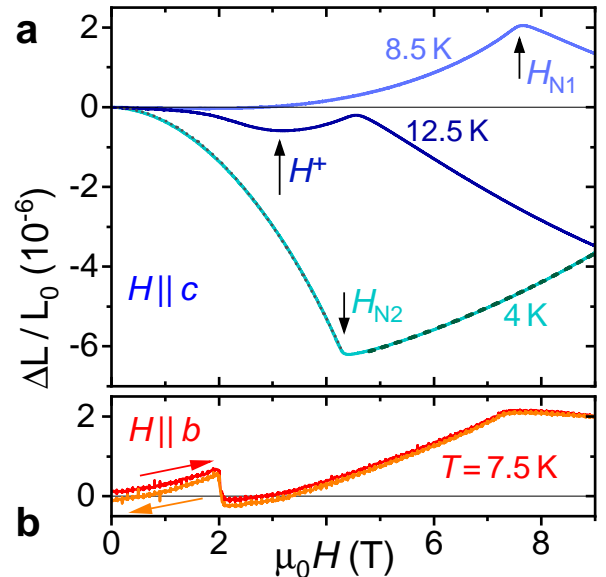


**Fig. 6.** Magnetostriction data. **a**  $\Delta L(H)/L_0$  for  $\mathbf{H} \parallel c$  and three exemplary temperatures. The dotted black line at 4 K is a fit to  $\Delta L(H)/L_0 = a'H^2$  (see text), and the dashed one to  $a''H^2 + c''$ , see Supplementary Note 5. **b**  $\Delta L(H)/L_0$  for  $\mathbf{H} \parallel b$ . Data for field sweep up (red) and down (orange) show a tiny hysteresis. A spin-flop takes place at  $H_m^b \approx 2$  T.

entering region I for fields above  $H_{N2}$ : the sample now expands along  $c$  with increasing  $H$  or  $T$ . We emphasize that the  $H^2$ -dependence of the magnetostriction inside region I, dashed line in Fig. 6a, is consistent with an expected expansion of fm polarons, see Supplementary Note 5. Unfortunately, with a maximum field of 9 T along the  $c$  axis we do not reach  $H_{N1}$  at 4 K.

At 8.5 K,  $\Delta L(H)/L_0$  is negligibly small up to  $\sim 2.5$  T. This can be explained by a concurrence of sizeable moment fluctuations at zero field in this  $T$ -range, seen e.g. by muon spin rotation measurements ( $\mu$ SR) [23], and a fm alignment of magnetic moments with field, as will be discussed below. The latter prevails at higher fields and the sample expands with  $H$ , as expected for region I from the 4 K-data. Between 5 T  $\lesssim \mu_0 H \lesssim 7.4$  T, a  $H^2$ -law holds again. Above  $H_{N1}$ , i.e. in the paramagnetic regime, fluctuations are suppressed by magnetic field and the sample contracts.

An intriguing behavior is observed at  $T = 12.5$  K. The sample initially contracts, but crosses over into expansion at  $H^+$  before a sharp transition into contraction is observed for  $H > H_{N1}$ . According to these dilatation data the minimum at  $H^+$  indicates a crossover from region III into I of the phase diagram Fig. 5c, in contrast to the sharp transitions at  $H_{N1}$  and  $H_{N2}$ . Likely, it is this crossover behavior that hindered a clear-cut assignment in other measurements [16, 23]. It should be noted that the slopes of  $\Delta L^{001}(H)/L_0$  just below  $H^+$  as well as above  $H^+$  are comparable for the different temperatures.

### Thermal expansion at low temperatures

The values of  $\alpha^{100}$  and  $\alpha^{001}(T, H = 0)$  show a qualitatively similar behavior but with opposite sign, cf. Fig. 4b and its inset (see also Supplementary Note 3 and Supplementary Figure 4). Likewise, the magnetostrictions along  $a$  and  $c$ , Figs. 4c and 6a, exhibit qualitatively very similar behavior, yet again with opposite sign. However, the effects are much larger along  $a$  compared to  $c$ . In addition, the magnetostriction  $\Delta L^{100}(H)$  does not follow an  $H^2$ -dependence even below  $T_{N2}$  as can be inferred from the coefficient  $\lambda$  in Fig. 4d. This behavior can be attributed to the complex magnetic structure of  $\text{Eu}_5\text{In}_2\text{Sb}_6$ . The magnetization  $M^{100}(H)$  exhibits a metamagnetic behavior [16]; in case of the example at 4 K this takes place just below 1.5 T, see Fig. 7a.  $H_{N2}$  may then be related to a spin-flop transition within the additional afm order below  $T_{N2}$  with ordered moments along  $a$  [22, 23]. The very sharp, almost jump-like increase of  $\Delta L^{100}(H)$  near  $H_{N2}$  at lowest temperatures supports such a scenario which, in turn, explains the deviation of  $\Delta L^{100}(H)$  from a  $H^2$ -dependence.

Fully relativistic density functional theory (DFT) calculations predict the ground state of  $\text{Eu}_5\text{In}_2\text{Sb}_6$  to be close to an afm A-type configuration with the Eu spin moments in the  $ab$ -plane and antiparallel stacking

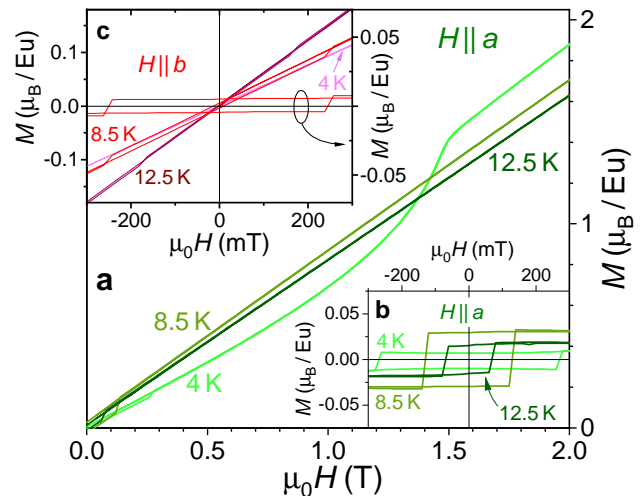


**Fig. 7. Magnetization curves  $M(H)$  for selected  $T$  and  $H$ .** **a** At 4 K, a metamagnetic transition is observed for  $\mathbf{H} \parallel a$ . **b** Low-field zoom of data with  $\mathbf{H} \parallel a$  and linear slope subtracted showing hysteresis. **c**  $M(H)$  at low fields for  $\mathbf{H} \parallel b$ . A tiny hysteresis is seen at 8.5 K, as is more obvious once a linear slope is subtracted, right scale.

along  $c$  [15]. The easy magnetization direction is along  $b$  [14, 16]. Recent neutron data are consistent with this picture, particularly for  $T_{N2} \leq T \leq T_{N1}$  [22, 23]. Given the aforementioned relation of our dilatation data to the magnetic properties, it is then not surprising that  $\alpha^{010}(T)$  is small, see inset to Fig. 2a. The magnetostriction at 7.5 K is similarly small, red data in Fig. 6b. The magnetic structure facilitates a spin-flop transition which is clearly seen in  $\Delta L^{010}(H)$  at  $H_m^b \sim 2$  T.  $M(H)$  data revealed this spin-flop to occur at all  $T < T_{N1}$  [16]. In addition,  $\Delta L^{010}(H)$  again follows an  $H^2$ -dependency up to  $H_{N1} \sim 7.4$  T except near  $H_m^b$ . The small offset in length after a cycle of field up- and down-sweeps possibly results from different configurations of magnetic domains [34].

### Discussion

The thermal expansion coefficients  $\alpha^{010}(T, H)$ , inset to Fig. 2a, do not show an additional feature between  $T_{N2} \leq T \leq T_{N1}$  as it was seen along the  $a$  and  $c$  directions. With the Eu moments aligned along  $b$ , this provides a hint toward the origin of the additional crossover  $H^+$  in the  $a$ - and  $c$ -phase diagrams. As mentioned, there is sufficient evidence for polaron formation in  $\text{Eu}_5\text{In}_2\text{Sb}_6$  well above  $T_{N1}$  [14–16, 26, 27]. However, unlike in fm materials where the polarons are simply taken up with the onset of magnetic order [30, 35–38], in antiferromagnets the polarons may coexist with the material's global (long-range) order [35, 39–43]. Upon cooling  $\text{Eu}_5\text{In}_2\text{Sb}_6$  to below  $T_{N1}$ , the already existing polarons with their short-range fm interaction in the  $ab$  plane can most easily embed into the afm ordered environment with their mag-

netic moments oriented along  $b$ , as suggested by the fm chains along  $b$ , see sketch of moments in Fig. 2. Along  $b$  and in region I of the phase diagram, the fm polarons simply include a few reversed moments around the trapped conduction electron, cf. sketch in Fig. 5a and Ref. [41]. Of course, the alignment of magnetic moments between different fm polarons can still be opposite and hence, a net antiferromagnetism can be observed along  $b$ . Note that, despite the afm ground state, short-range fm interactions are relevant in  $\text{Eu}_5\text{In}_2\text{Sb}_6$  as evidenced by Curie-Weiss fits of the high-temperature susceptibility [14, 16]. It is this delicate balance of the two interactions—along with the gain in exchange energy—which allows fm polarons to easily form above  $T_{\text{N1}}$  [44, 45].

The situation is different for the  $a$  direction, Fig. 4. Below  $T_{\text{N1}}$ , the sample expands with decreasing  $T$ , a behavior observed in a few afm materials upon entering the ordered state [46, 47]. As a result of the intermediate magnetic anisotropy along  $a$ , the magnetization processes of the afm states are different compared to the  $b$  direction. In a simplified, two-sublattice picture of an antiferromagnet, a magnetic field along  $a$  or  $c$  results in a canting of the moments, and polarons with moment parallel  $\mathbf{H}$  will experience a different change of its surface energy as compared to those antiparallel moments. In consequence, the effective size of these polarons and their stability against thermal or quantum mechanical fluctuations will be changed. (Note that such differences in polaron-moment alignment do not take hold for field applied in easy  $b$  direction.) Such a stabilization is reflected by the suppression of the negative  $\alpha^{100}(T, H)$  just below  $T_{\text{N1}}$  with increasing fields up to  $\mu_0 H = 4$  T. Essentially, this picture of embedded ferromagnetic polarons should also hold for the more complex afm state of  $\text{Eu}_5\text{In}_2\text{Sb}_6$  in applied fields perpendicular to the easy axis. Hence, these high-field data suggest that in region I, fm polarons coexist with afm long-range order. This is corroborated by the negative magnetostriction  $\Delta L^{100}$  at higher fields in Fig. 4c indicating a suppression of afm fluctuations. The larger jump of  $\alpha^{100}(T, H)$  at  $T_{\text{N1}}$  and small fields, i.e. upon going from the paramagnetic into region III in the phase diagram, is then consistent with a prevailing afm transition at  $H_{\text{N1}}$  while the crossover at  $H^+$  marks the additional impact of fm polarons. The different afm order below  $H_{\text{N2}}$  with the magnetic moments along  $a$  [22, 23], region II, terminates the signatures of polaron existence as seen by the very strong changes in both thermal expansion and magnetostriction. The suggestion of a relieved competition between afm and fm correlations [23] is consistent with this scenario.

The twofold change of slope of the magnetostriction  $\Delta L(H)/L_0$  in Fig. 6a clearly indicates competing interactions and highly likely magnetic inhomogeneity. The resulting phase diagrams exhibit an unusual  $H^+$ -crossover line with increasing  $H$ -values for increasing  $T$  which cannot be explained by anisotropy effects alone [31, 33].

Rather, such an unexpected thermal behavior is predicted by a phenomenological model introduced in Supplementary Note 5. This model considers anisotropic polarons in an antiferromagnet and finds an increased stability of the fm polarons inside the global afm order upon decreasing temperature, i.e. upon going from region III to I. Concomitantly, the polarons' volume decreases. As a consequence of these two effects, the decreasing magnetization of the low-field hysteresis in Figs. 7b and c, which indicates a fm polaronic component, can be rationalized. In contrast, in the more common case of fm polarons in an eventually fm ordered material, the polarons would just dissolve upon entering the globally ordered state.

For fields along  $a$  and  $c$  large enough to drive the system close to the field-polarized paramagnetic state, polarons with moments opposite to the field direction cease to exist, leaving only polarons with parallel components along the field direction. The fact that the  $H^+$ -crossover lines end on the  $H_{\text{N1}}$ -lines in the magnetic phase diagrams, Fig. 5, in a field range comparable to the spin-flop field  $H_m^b$  for  $H \parallel b$  corroborates such a simple picture. Here, the Zeeman energy compensates the magnetic anisotropy.

The qualitatively complementary behavior along the  $a$  and  $c$  axis below  $T_{\text{N1}}$ , best seen in Fig. 4b and its inset, suggests similar short-range fm and long-range afm competition in the phase diagrams of these two directions. Hence, the above assignments of the regions I–III can be cross-compared with the magnetostriction results  $\Delta L(H)$  for  $\mathbf{H} \parallel c$  in Fig. 6a. At 4 K, the initial decrease of  $\Delta L(H)$  marks afm region II, while its increase above  $H_{\text{N2}}$  in region I (a behavior similar to the one observed before [48]) signals the incorporation of fm polarons. At 8.5 K, long-range afm and short-range fm correlations coexist and compete, which causes the initially negligible  $\Delta L(H)$ . Increasing  $H$  favors the fm arrangement and  $\Delta L(H)$  increases. An increasing volume upon going from a preferred afm to a fm moment configuration was observed e.g. in  $(\text{Hf}, \text{Ta})\text{Fe}_2$  [49]. In the paramagnetic regime beyond  $H_{\text{N1}}$  the field suppresses magnetic fluctuations and  $\Delta L(H)$  decreases. At 12 K, the afm order gives rise to the contraction of the sample in region III, which smoothly crosses over into an expansion above  $H^+$ , where polarons appear to exist more easily. The paramagnetic state above  $H_{\text{N1}}$  is again accompanied by a negative  $\lambda$ .

Interestingly, the temperature  $T^+$  corresponds to the steepest decrease in  $r(T)$  upon decreasing  $T$  (Fig. 3) consistent with its assignment as a crossover. A strong decrease of resistivity near 10.5 K in zero field was also reported earlier [23]. We emphasize that the slopes of  $r(T)$  just above  $T_{\text{N1}}$  and somewhat below  $T^+$  coincide, as indicated by the dotted line in Fig. 3. This is highly suggestive of polarons continuing to exist below the onset of afm order at  $T_{\text{N1}}$  and both phenomena operating relatively independent of each other.

A physical picture of electronic transport in  $\text{Eu}_5\text{In}_2\text{Sb}_6$  has to incorporate the existence of self-trapped fm polarons within the afm phases, which generates a magnetically and electronically inhomogeneous behavior. DFT results [15] suggested  $\text{Eu}_5\text{In}_2\text{Sb}_6$  to be a semimetal with small Fermi sheets. The availability of charge carriers was found to depend strongly on the spin configuration, with the fm state having a strongly enhanced density of states (DOS) at the Fermi level  $E_F$  compared to (collinear) afm configurations. The suppression of the fm polaron volume towards lowest  $T$  decreases the availability of charge carriers, while the magnetically inhomogeneous and noncollinear configuration in the ground state impedes electronic transport. This explains both the strong increase of  $\rho(T)$  at lowest temperatures and the remarkably large magnetoresistance. In particular, the magnetoresistive properties appear to be similar to those observed in metallic granular magnetoresistive materials [50, 51]. An alternative picture arises in insulating or semiconducting materials where charge carriers (stemming solely from defects) are dressed as fm polarons and are exclusively responsible for electronic transport. The observed behavior of  $\rho(T)$  upon lowering  $T$  should then be explained by the density of polarons and eventually by increased magnetic scattering of the mobile fm polarons in the afm matrix. We emphasize that both scenarios rely on the existence of fm polarons and the self-trapping of charge carriers both in the paramagnetic and within the afm ordered states. Further investigations of electronic band structure are needed here.

Our thermal expansion measurements reveal a strongly anisotropic behavior of  $\text{Eu}_5\text{In}_2\text{Sb}_6$  and nicely confirm the existence of anisotropic polarons well above  $T_{N1}$ . In particular, an enhanced DOS at near  $E_F$  inside the ferromagnetically ordered polarons [15] provides an explanation for the huge negative magnetoresistance in  $\text{Eu}_5\text{In}_2\text{Sb}_6$  which differs from the double-exchange mechanism in CMR manganites [6]. In the antiferromagnetically ordered phase below  $T_{N1}(H)$  the magnetostriction results point to a coexistence of global afm order with fm polarons, with the latter being stabilized upon decreasing temperature. In contrast, there is no indication for polarons below  $T_{N2}(H)$ . The insight into polaronic behavior provided here may help in advancing CMR effects in materials suited for applications.

## Methods

Single crystals of  $\text{Eu}_5\text{In}_2\text{Sb}_6$  were grown by a combined In-Sb self-flux technique [14]. Here we report results obtained on the same crystals as those investigated earlier [16] (additional samples investigated here came from the same batch). The crystallographic orientation of the single crystals was determined by a real-time Laue X-ray system (Laue-Camera GmbH [52]), see also Fig. 1e in Ref. [15] and Supplementary Note 1 and Supplementary

Figure 1.

For thermal expansion and magnetostriction measurements a dilatometer cell was employed [53]. The cell was equipped with a Cernox temperature sensor providing an accuracy of better than  $\pm(10\text{ mK} + T/1000)$ . The measurements were conducted in a Physical Property Measurement System (PPMS) by Quantum Design Inc. [54] with a maximum magnetic field of 9 T applied parallel to the sample direction along which the dilatation was measured. Special attention was paid to minimize electrical noise [55]. Thermal expansion measurements were conducted upon warming the sample (if not stated otherwise) and repeated at least once for comparison. The error of the measured relative length changes  $\Delta L/L_0$  in thermal expansion and magnetostriction was estimated to  $\leq 10^{-6}$ . The error bar of the calculated absolute values of the thermal expansion coefficients  $\alpha$  amounts to about  $5 \cdot 10^{-7} \text{ K}^{-1}$ . This may account for the apparent low-temperature offsets, particularly along the  $b$  direction for which the sample dimension was smallest (see Supplementary Figure 1). Before each magnetostriction measurement the sample was heated up to at least 100 K to avoid any influence of the magnetic history of the sample. Unfortunately, the samples often broke inside our measurement cell, specifically upon applying magnetic fields, a fact that severely limited the number of results obtained at higher fields.

Magnetization measurements were conducted in a Magnetic Property Measurement System (MPMS3) by Quantum Design Inc. [54] with an accuracy of better than  $0.004 \mu_B/\text{Eu}$ .

## Appendix

### 1. $\text{Eu}_5\text{In}_2\text{Sb}_6$ samples

Supplementary Fig. 8 shows the dimensions and orientation of one of our  $\text{Eu}_5\text{In}_2\text{Sb}_6$  samples (sample length along the shortest,  $b$  direction is approximately 0.46 mm) which is typical for the samples investigated in this study. In line with our earlier findings [15], the  $ab$  planes are usually well defined implying that sample mounting for dilatation measurements along  $c$  is straightforward. However, care must be taken due to the rod-like shape of the samples which often caused the samples to break during the experiments. In contrast, the samples did often not exhibit well defined  $ac$  and  $bc$  planes which rendered sample mounting difficult for dilatation measurements along  $b$  and  $a$ , respectively. Again, samples often cracked after measurements leaving the corresponding results unreliable.

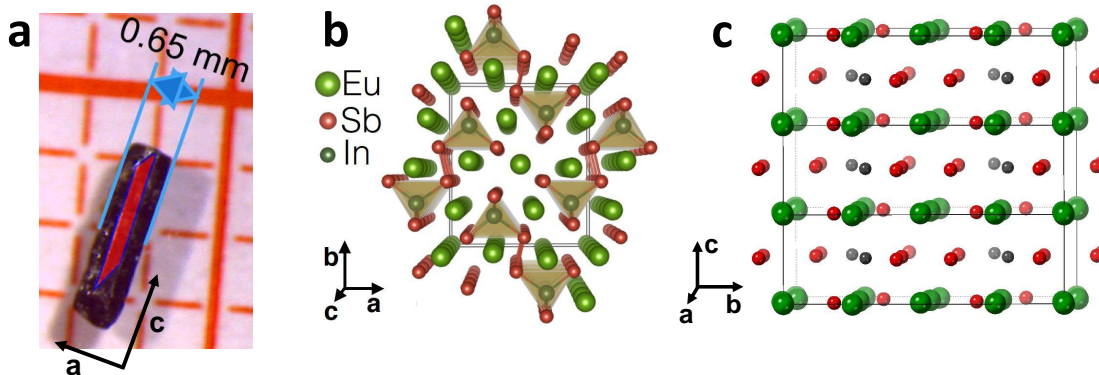


**Fig. 8.  $\text{Eu}_5\text{In}_2\text{Sb}_6$  samples.** **a** Photograph of a typical  $\text{Eu}_5\text{In}_2\text{Sb}_6$  sample used in this study. The crystallographic orientation was determined by Laue diffraction measurements. All samples are rod-like shaped with the long dimension corresponding to the crystallographic  $c$  direction. The topmost  $ac$  plane of the sample is marked in red. **b** and **c** Perspective view of the orthorhombic crystal structure of  $\text{Eu}_5\text{In}_2\text{Sb}_6$  along the  $[001]$  and the  $[100]$  axis, respectively. In **b**, the three groups of crystallographically unique Eu atoms,  $\text{Eu}(1)$ ,  $\text{Eu}(2)$ , and  $\text{Eu}(3)$ , are marked. Figure part **b** taken from Ref. 15.

## 2. Fitting the thermal expansion data

In the following, we present detailed results obtained by using different models to fit our thermal expansion data measured along different crystallographic directions.

### Semiclassical model

For fitting our data to the model developed by Mukherjee *et al.* [24, 56] we made use of the formulae provided there for the change of length:

$$\frac{\Delta L}{L_0} = \frac{\langle \xi \rangle_T - \langle \xi \rangle_{T_0}}{L_{T_0}}. \quad (1)$$

Here,  $L_{T_0}$  is the length of the sample at reference temperature  $T_0$ . The average lattice displacement  $\xi$  at a given temperature is [56]:

$$\langle \xi \rangle_T = \gamma T^2 + \frac{3g}{4c^2} \left[ 3k_B T \left( \frac{T}{\theta_D} \right)^3 \int_0^{\theta_D/T} \frac{z^3 dz}{e^z - 1} - \frac{3f}{4c^2} \left( 3k_B T \left( \frac{T}{\theta_D} \right)^3 \int_0^{\theta_D/T} \frac{z^3 dz}{e^z - 1} \right)^2 \right] \quad (2)$$

For simplicity, we used  $u = \frac{3g}{4c^2} 3k_B$  and  $v = \frac{9gf}{16c^4} (3k_B)^2$  when conducting the fits. Also, a vertical offset of the fitted curves were allowed. The results of the fitting procedure are listed in the following Table I and some fitted curves are included in Figure 1 of the main text (dashed lines).  $T_{min}$  refers to the minimum temperature for which data were included in the respective fitting procedure. The maximum temperature of data used in the fitting was 130 K.

### Parabolic fits

For simplicity, we also attempted to fit our thermal expansion data to a parabolic function  $\Delta L(T)/L_0 =$

TABLE I. Fit parameters obtained by fitting  $\Delta L(T, H)$  to the model described by Mukherjee *et al.* [56]. For simplicity,  $\theta_D = 197$  K was fixed [16].

data			fit parameter				
data set	direction	$\mu_0 H$ T	offset $10^{-6}$	$\gamma$ $10^{-9} \text{K}^{-2}$	$u$	$v$	$T_{min}$ K
36A	(100)	0	4.7	36	41.3	0.62	22.8
42B	(100)	0.5	0.5	40	40.0	0.59	23.5
40B	(100)	1.0	-3.1	40	38.6	0.61	22.6
41B	(100)	1.5	-16.3	44	35.9	0.60	23.6
39B	(100)	2.0	-30.1	48	33.8	0.62	22.8
38B	(100)	3.0	-16.8	57	29.2	0.66	22.9
37B	(100)	4.0	-0.7	62	26.8	0.73	16.8
191022	(001)	0	-0.5	0	23.3	-0.48	30.5

$c + aT^2$ . The resulting fitting parameters are listed in Table II. The fitted curves are presented in Fig. 9.

TABLE II. Fit parameters obtained by fitting the thermal expansion data to  $\Delta L(T)/L_0 = c + aT^2$ . Here,  $\Delta L(T)$  was measured for different directions and magnetic fields.  $T_{min}$  denotes the minimum temperature of data included in the fit.

data			fit parameter		
data set	direction	$\mu_0 H$ T	$c$ $10^{-6}$	$a$ $\text{K}^{-2}$	$T_{min}$ K
36A	(100)	0	-5.9	0.0905	55.0
42B	(100)	0.5	-7.5	0.091	55.0
40B	(100)	1.0	-10.9	0.0915	55.6
41B	(100)	1.5	-21.9	0.0912	54.5
39B	(100)	2.0	-33.2	0.0913	54.5
38B	(100)	3.0	-13.3	0.0915	55.0
37B	(100)	4.0	+8.5	0.0918	55.0
241022	(010)	0	-39.3	0.0626	48.0
191022	(001)	0	-63.8	0.0517	58.0

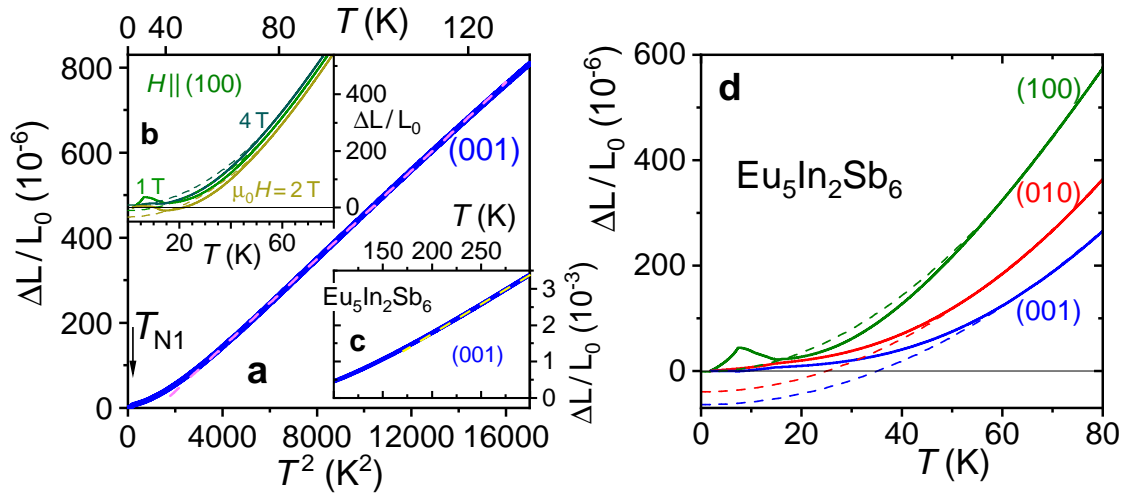


**Fig. 9. Fit of the thermal expansion data to parabolas.** **a**  $\Delta L^{001}(H)/L_0$  plotted on a  $T^2$ -scale to exemplify the quality of the fit up to 130 K. **b**  $T^2$ -fits to data obtained at applied magnetic fields. **c** At  $T \gtrsim 175$  K a linear expansion is found (as discussed in the main text). **d** Examples of parabolic fits with focus on temperatures below 80 K. The inset shows exemplary fits to data obtained at finite magnetic fields along (100). The parameters obtained from the fits are summarized in Supplementary Table II. The error of the measured relative length changes  $\Delta L/L_0$  was estimated to  $\leq 10^{-6}$ .

### Fits of polynomials of 4th order

In addition, the thermal expansion data are fitted by using polynomials of fourth order. The results of these fits are presented in Table III. Note that linear terms have been omitted. The fitted curves are shown in Fig. 10.

TABLE III. Fit parameters obtained by fitting the thermal expansion data at zero field to  $\Delta L(T)/L_0 = \sum_{i=0}^4 a_i T^i$ .  $T_{min}$  denotes the minimum temperature of data included in the fit. The linear coefficient was set to  $a_1 = 0$ .

data		fit parameter				
data set	direction	$a_0$ $10^{-6}$	$a_2$ $10^{-9}$ $K^{-2}$	$a_3$ $10^{-10}$ $K^{-3}$	$a_4$ $10^{-12}$ $K^{-4}$	$T_{min}$ K
36A	(100)	-22.4	72.4	8.1	-7.0	32.0
241022	(010)	10.8	3.2	10.6	-5.1	30.2
191022	(001)	-1.7	1.6	7.4	-3.0	33.4

### 3. Thermal expansion data measured along the $b$ and $c$ crystallographic direction

Some thermal expansion data measured along the  $b$  and  $c$  crystallographic directions are shown in Fig. 11.

### 4. Additional magnetostriction data

In an effort to increase reliability, the thermal expansion and magnetostriction measurements were conducted

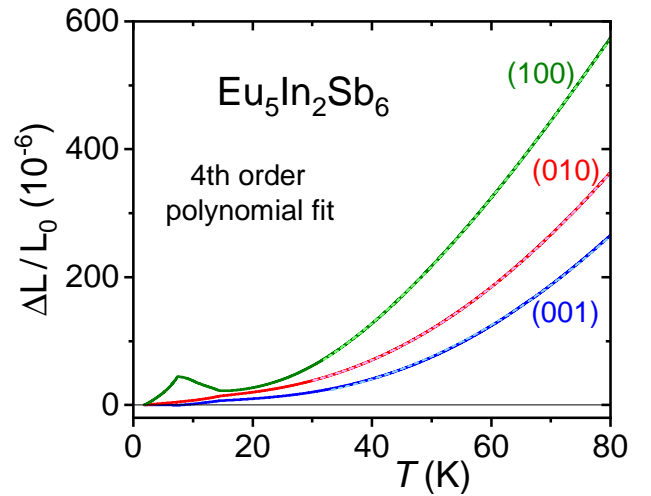


**Fig. 10. Fit of the thermal expansion data to polynomials of fourth order.** Fitted curves are shown as light dashed lines. The parameters obtained from the fits are summarized in Supplementary Table III. The error of  $\Delta L/L_0$  is  $\leq 10^{-6}$ .

on several samples and by using two different measurement setups. In addition to the data shown in the main text, we report in Fig. 12 magnetostriction data obtained by means of another setup for  $\vec{H} \parallel b$ . The corresponding results are included in the phase diagram Figure 5b of the main text as dotted triangles. Clearly, these data fit excellently into the phase diagram.

Thermal expansion and magnetostriction measurements shown in this Note were performed using a capacitance dilatometer in a  $^4\text{He}$  cryostat[57]. All thermal expansion measurements were performed using a slow con-

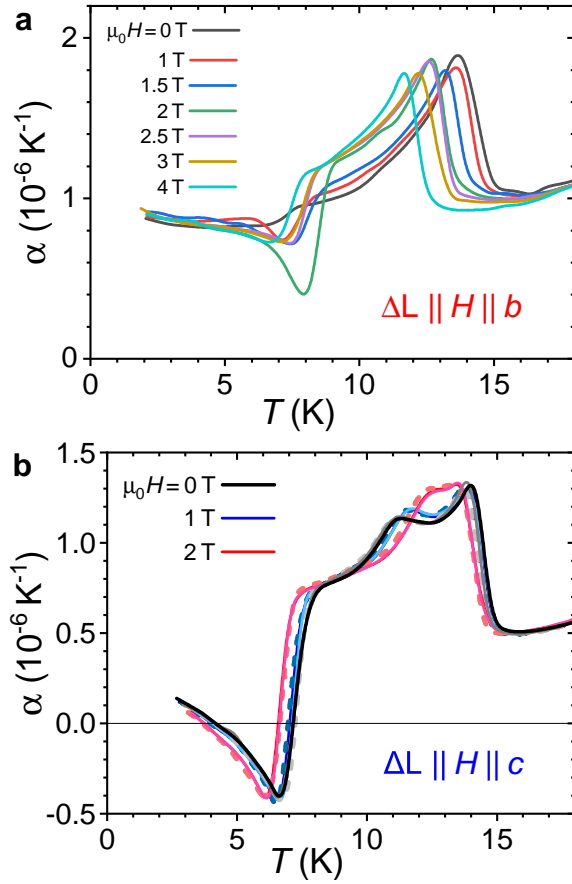


**Fig. 11. Thermal expansion coefficients  $\alpha$**  measured along **a** the crystallographic  $b$  direction and **b** the  $c$  direction. In **b**, results of three consecutive runs for each field value (0 T, 1 T, 2 T) are presented by lines of similar colors; full lines: sample warming up to 100 K, dashed lines: sample cooling down. Errors bars of  $\alpha$  amount to about  $5 \cdot 10^{-7} \text{ K}^{-1}$ .

tinuous temperature ramp, whereas all magnetostriction measurements were performed by stabilizing the field to avoid the influence of eddy currents. Thermal expansion data were corrected by performing a background subtraction of the cell effect under identical thermal conditions.

## 5. Description of anisotropic polarons

### Anisotropic polarons in an anisotropic antiferromagnet

Hereinafter, we closely follow the procedure of Kagan *et al.* [43]. Due to the anisotropy in the exchange coupling and the hopping of the conduction electrons the polarons are assumed to have ellipsoidal shape with axes

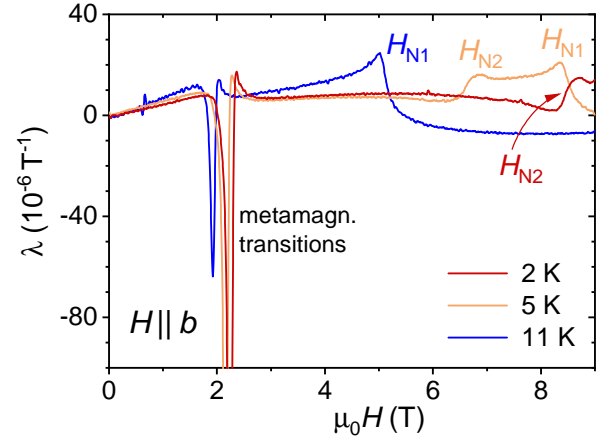


**Fig. 12. Magnetostriction coefficient  $\lambda$**  measured with  $\mathbf{H} \parallel b$  at three different temperatures.

$\{R_x, R_y, R_z\}$ . We consider the Hamiltonian

$$\hat{\mathcal{H}} = -J_H \sum_i \vec{S}_i \cdot \vec{\sigma}_i + \sum_{\langle ij \rangle_\alpha} J_\alpha (\vec{S}_i \cdot \vec{S}_j + S^2) - \sum_{\langle ij \rangle_\alpha \sigma} t_\alpha (c_{i\sigma}^\dagger c_{j\sigma} + H.c.) \quad (3)$$

on a simple cubic lattice structure of the antiferromagnetic material. Here,  $J_H$  is the Hund's rule interaction which locally couples ferromagnetically the spin  $\vec{S}$  with the spin of the electron  $\vec{\sigma}$ ,  $J_\alpha$  is the nearest neighbor exchange coupling in the direction  $\alpha = \{x, y, z\}$ , and  $t_\alpha$  the nearest neighbor hopping amplitude along the  $\alpha$ -direction. We assume  $J_H \gg \{t_x, t_y, t_z\} \gg \{J_x, J_y, J_z\}$  and denote the intersite distance with  $a$ . The exchange energy has been shifted such that the antiferromagnetic state has zero energy. The spins are semiclassical,  $\vec{S} = 2S\vec{\sigma}$ , i.e. they correspond to a spin 1/2 with the length of a spin  $S$ .

A prerequisite for polaron formation is a low enough carrier concentration. The dispersion of the conduction band is small, so that the electrons are spread over the entire polaron. We consider two interpenetrating sublattices, A and B, with up- and down-spins, respectively. Due to the Hund's rule coupling the sublattices provide up-spin and down-spin charge carriers, respectively. A very small magnetic field polarizes the conduction band.

An ellipsoidal polaron has a dimensionless volume of  $\Omega_{\text{ell}} = \frac{4\pi}{3} \frac{R_x R_y R_z}{a^3}$  and a polarization energy of

$$E_{\text{pol}} = 2(J_x + J_y + J_z)S^2 n \Omega_{\text{ell}} = 2(J_x + J_y + J_z)S^2 n (4\pi/3) \frac{R_x R_y R_z}{a^3}, \quad (4)$$

that arises from the exchange energy of  $2J_\alpha S^2$  per bond inside the ellipsoid, while the exchange energy at the surface boundary vanishes. The conduction electrons inside

the polaron have carrier density  $n$  and their spins aligned either all up or all down.

The kinetic energy of the band of conduction states with nearest neighbor hopping is

$$\varepsilon(\vec{k}) = -2 \left[ t_x \cos(k_x a) + t_y \cos(k_y a) + t_z \cos(k_z a) \right]. \quad (5)$$

Expanding for small  $\vec{k}$  we have

$$\begin{aligned} \varepsilon(\vec{k}) &= -2(t_x + t_y + t_z) + [t_x(k_x a)^2 + t_y(k_y a)^2 + t_z(k_z a)^2] \\ &\rightarrow -2(t_x + t_y + t_z) - a^2 \left[ t_x \frac{\partial^2}{\partial x^2} + t_y \frac{\partial^2}{\partial y^2} + t_z \frac{\partial^2}{\partial z^2} \right]. \end{aligned} \quad (6)$$

For simplicity, we rescale the coordinates  $\tilde{y} = y \sqrt{\frac{t_x}{t_y}}$  and  $\tilde{z} = z \sqrt{\frac{t_x}{t_z}}$  so that

$$R_x = \tilde{R}_x = \tilde{R}_y = R_y \sqrt{\frac{t_x}{t_y}} = \tilde{R}_z = R_z \sqrt{\frac{t_x}{t_z}}$$

and

$$\nabla_{\tilde{r}}^2 = \frac{\partial^2}{\partial \tilde{r}^2} + \frac{2\partial}{\tilde{r}\partial \tilde{r}} \quad (7)$$

Without loss of generality, we assumed  $t_x > \{t_y, t_z\}$  resulting in  $R_x$  being the largest axis of ellipsoid and

$$\hat{\mathcal{H}}_{\text{kin}} = -a^2 t_x \left[ \frac{\partial^2}{\partial x^2} + \frac{\partial^2}{\partial \tilde{y}^2} + \frac{\partial^2}{\partial \tilde{z}^2} \right] = -a^2 t_x \nabla_{\tilde{r}}^2. \quad (8)$$

The Schrödinger equation is

$$\hat{\mathcal{H}}_{\text{kin}} \psi(\vec{r}) = -a^2 t_x \nabla_{\tilde{r}}^2 \psi(\vec{r}) = \varepsilon_0 \psi(\vec{r}), \quad (9)$$

where  $\varepsilon_0$  is the ground state energy. The ground state wave function in the polaron  $\psi(\vec{r}) = \frac{\sin(k\vec{r})}{k\vec{r}} = j_0(k\vec{r})$  should vanish at the surface of the ellipsoid so that  $k = \pi/\tilde{R}$ . The ground state energy is then

$$\varepsilon_0 = t_x a^2 (\pi/R_x)^2. \quad (10)$$

We assume that the charge density is dilute enough so that all the electrons can be accommodated into the ground state. The kinetic energy and the total energy are then given by

$$E_{\text{kin}} = -2(t_x + t_y + t_z)n + t_x a^2 (\pi/R_x)^2 n \quad (11)$$

$$\begin{aligned} E_{\text{tot}} &= E_{\text{pol}} + E_{\text{kin}} = -2(t_x + t_y + t_z)n + t_x a^2 (\pi/R_x)^2 n \\ &\quad + 2(J_x + J_y + J_z)S^2 n (4\pi/3) \left( \frac{R_x}{a} \right)^3 \frac{\sqrt{t_y t_z}}{t_x}. \end{aligned} \quad (12)$$

With the notations  $\tilde{J} = (J_x + J_y + J_z)S^2$  and  $t_{\text{eff}} = (t_x t_y t_z)^{1/3}$  we find

$$\begin{aligned} E_{\text{tot}} &= -2(t_x + t_y + t_z)n + t_x \pi^2 (a/R_x)^2 n \\ &\quad + 2\tilde{J}n(4\pi/3) \left( \frac{R_x}{a} \right)^3 \left( \frac{t_{\text{eff}}}{t_x} \right)^{3/2}. \end{aligned} \quad (13)$$

The minimization of the total energy with respect to  $R_x/a$  yields for the large axis of the ellipsoid

$$R_x/a = \left( \frac{\pi t_x^2}{4\tilde{J}\sqrt{t_y t_z}} \right)^{1/5} = \left[ \frac{t_x \pi}{4\tilde{J}} \left( \frac{t_x}{t_{\text{eff}}} \right)^{3/2} \right]^{1/5} \quad (14)$$

$$\begin{aligned} \Omega_{\text{ell}} &= \frac{4\pi}{3} \frac{R_x R_y R_z}{a^3} = \frac{4\pi}{3} \left( \frac{R_x}{a} \right)^3 \sqrt{\frac{t_y t_z}{t_x^2}} \\ &= \frac{4\pi}{3} \sqrt{\frac{t_y t_z}{t_x^2}} \left( \frac{\pi t_x^2}{4\tilde{J}\sqrt{t_y t_z}} \right)^{3/5} = \frac{\pi^{8/5} 2^{4/5}}{3} \left( \frac{t_{\text{eff}}}{\tilde{J}} \right)^{3/5} \end{aligned} \quad (15)$$

Hence, the energy of an ellipsoidally shaped polaron amounts to

$$\begin{aligned} E_{\text{tot}} &= -nJ_H S - 2(t_x + t_y + t_z)n + t_x \pi^2 (a/R_x)^2 n \\ &\quad + 2\tilde{J}n(4\pi/3) \left( \frac{R_x}{a} \right)^3 \left( \frac{t_{\text{eff}}}{t_x} \right)^{3/2}. \end{aligned} \quad (16)$$

All terms of the total energy are proportional to  $n$ . These results are in agreement with those by Kagan *et al.* [43].

### Anisotropic polarons in a magnetic field (Zeeman splitting)

In the following, we assume that the magnetic field is applied either parallel or antiparallel to the ferromagnetic moment of the elliptical polaron giving rise to opposite signs of the Zeeman energy of the charge carriers

$$E_{\text{kin}} = -2(t_x + t_y + t_z)n + t_x \pi^2 (a/R_x)^2 n \mp g_e \frac{H}{2} n. \quad (17)$$

We now consider the polarization of the antiferromagnetic lattice, which, again, is subdivided in sublattices A and B with up-spins and down-spin, respectively. The ground state of the antiferromagnetic (afm) phase yields  $S_{\text{eff}} = 0$ . The Zeeman splitting energy is given by  $+g_S H \sum_j S_j^z$ , where the sum is over the sublattices A and B. There is a continuum of magnetic excitations above the ground state singlet. In the afm bulk material, the additional (field-dependent) term of the energy is then  $\frac{1}{2} H^2 \chi_{\parallel, \perp}$ , where the susceptibility  $\chi \propto 1/\tilde{J}$ . This term is small and can be neglected.

The magnetic energy of the ellipsoidal polaron is  $\pm g_S S H \Omega_{\text{ell}}$  and it follows (proceeding as above) [58]

$$\begin{aligned} E_{\text{pol}}^{\pm} &= (4\pi/3) \left( \frac{R_x}{a} \right)^3 \left( \frac{t_{\text{eff}}}{t_x} \right)^{3/2} \left( 2\tilde{J}n \mp g_S S H \right) \\ E_{\text{tot}}^{\pm} &= -2(t_x + t_y + t_z)n + t_x \pi^2 (a/R_x)^2 n \mp g_e \frac{H}{2} n \\ &\quad + (4\pi/3) \left( \frac{R_x}{a} \right)^3 \left( \frac{t_{\text{eff}}}{t_x} \right)^{3/2} \left( 2\tilde{J}n \mp g_S S H \right) \end{aligned} \quad (18)$$

The minimization of the total energy with respect to

$R_x/a$  yields the radius  $R_x/a$

$$\begin{aligned} \frac{\partial E_{\text{tot}}^{\pm}}{\partial(R_x/a)} &= 0 = -2t_x\pi^2(a/R_x)^3n + 4\pi(R_x/a)^2\left(\frac{t_{\text{eff}}}{t_x}\right)^{3/2}\zeta \\ R_x^{\pm}/a &= \left[\frac{\pi t_x}{4\tilde{J}}\left(\frac{t_x}{t_{\text{eff}}}\right)^{3/2}\right]^{1/5}\left(\frac{\zeta}{2\tilde{J}n}\right)^{-1/5} \\ \Omega_{\text{ell}}^{\pm} &= \frac{4\pi R_x R_y R_z}{3a^3} \\ &= \frac{4\pi}{3}\sqrt{\frac{t_y t_z}{t_x^2}}\left(\frac{\pi t_x^2}{4\tilde{J}\sqrt{t_y t_z}}\right)^{3/5}\left(\frac{\zeta}{2\tilde{J}n}\right)^{-3/5} \\ &= \frac{\pi^{8/5}2^{4/5}}{3}\left(\frac{2nt_{\text{eff}}}{\zeta}\right)^{3/5} \end{aligned} \quad (19)$$

where  $\zeta = 2\tilde{J}n \mp g_S S H$ . This way we obtain the total energy of a polaron in magnetic field

$$\begin{aligned} E_{\text{tot}}^{\pm} &= -nJ_H S - 2(t_x + t_y + t_z)n \\ &\quad \mp g_e \frac{H}{2}n + 2^{4/5}\frac{5}{3}\pi^{8/5}t_{\text{eff}}^{3/5}n\left(\frac{\zeta}{2n}\right)^{2/5} \end{aligned} \quad (21)$$

from which the magnetization and susceptibility of the polaron is calculated

$$\begin{aligned} m^{\pm} &= -\frac{\partial E_{\text{tot}}^{\pm}}{\partial H} \\ &= \pm g_e \frac{n}{2} \pm 2^{4/5}\frac{1}{3}\pi^{8/5}t_{\text{eff}}^{3/5}\tilde{J}^{-3/5}g_S S \left(\frac{\zeta}{2\tilde{J}n}\right)^{-3/5} \\ \chi^{\pm} &= \frac{\partial m^{\pm}}{\partial H} = 2^{-1/5}\frac{1}{5}\pi^{8/5}t_{\text{eff}}^{3/5}\tilde{J}^{-8/5}\frac{(g_S S)^2}{n}\left(\frac{\zeta}{2\tilde{J}n}\right)^{-8/5} \end{aligned} \quad (22)$$

Polarons with their spins aligned parallel to the magnetic field,  $E^+$ , have lower energies, are of larger size and have larger magnetization compared to those with antiparallel alignment,  $E^-$ , as well as  $\chi^+ > \chi^-$ . Note that  $\Omega_{\text{ell}}^+$ ,  $m^+$  and  $\chi^+$  diverge when  $g_S S H \rightarrow 2\tilde{J}n$  and the entire sample is field-polarized. For fields smaller than the one required for sample polarization, at finite temperature, a mixture of  $E^+$  and  $E^-$  polarons with opposite magnetization is present in the material.

It is important to note that a softening of the antiferromagnet, e.g. by increasing the temperature or the magnetic field, results in a reduction of  $\tilde{J}$ . Consequently,  $\Omega_{\text{ell}}$  increases with  $T$  while the polaron's energy decreases. The polarons grow in size but become less stable with increasing  $T$ . Hence, the magnetization and the susceptibility increase as well.

We also note that the polaron's zero-field energy is proportional to the carrier density  $n$ , while its zero-field magnetization (neglecting  $g_e n/2$ ) is independent of  $n$ . On the other hand, the susceptibility at  $H = 0$  is

inversely proportional to  $n$ .

### Magnetostriction of polarons

Within the present model the magnetostriction is isotropic in magnetic field,

$$\frac{R_x^{\pm}(H) - R_x^{\pm}(0)}{R_x^{\pm}(0)} = \frac{R_y^{\pm}(H) - R_y^{\pm}(0)}{R_y^{\pm}(0)} = \frac{R_z^{\pm}(H) - R_z^{\pm}(0)}{R_z^{\pm}(0)}.$$

At  $T = 0$ , all the polarons are of the  $E^+$ -type and, importantly, they expand with field. At finite temperature both types of polarons populate the system and the magnetostriction is given by

$$\frac{\Delta L(H)}{L_0} \propto \frac{N^+}{N} \frac{R_x^+(H) - R_x^+(0)}{R_x^+(0)} + \frac{N^-}{N} \frac{R_x^-(H) - R_x^-(0)}{R_x^-(0)}, \quad (24)$$

where  $N^+$  and  $N^-$  are the number of polarons of the  $E^+$ - and  $E^-$ -type, and  $N = N^+ + N^-$  is the total number of polarons.

The polarons of  $E^-$ -type compress under an applied magnetic field, but less than the expansion of the  $E^+$ -polarons. In particular, an expansion of eq. (24) by using eq. (19) for small enough magnetic fields,  $g_S S H/2\tilde{J}n \ll 1$ , results in an  $H^2$ -dependence of the magnetostriction to lowest order because linear-in- $H$  terms cancel out. Our experimental data at  $T = 4$  K and for  $\vec{H} \parallel c$  are consistent with such a description, see Fig. 6 of the main text: The data can nicely be fitted by  $\Delta L^{001}(H)/L_0 = a''H^2 + c''$  within the field range  $4.8 \text{ T} \leq \mu_0 H \leq 9 \text{ T}$ , where  $a'' = 4.25 \cdot 10^{-8} \text{ T}^{-2}$  and  $c'' = -7.1 \cdot 10^{-6}$ .

### Thermal equilibrium

We introduce Boltzmann factors for  $N^{\pm}$  and  $E^{\pm}$  and the partition function [58]

$$\frac{N^{\pm}}{N} = e^{-E^{\pm}/T} \quad \text{and} \quad \mathcal{Z} = e^{-E^+/T} + e^{-E^-/T}. \quad (25)$$

Making use of the definitions  $\Delta = E^- - E^+$  and  $E^0 = (E^- + E^+)/2$  we have

$$\begin{aligned} E^{\mp} &= E^0 \pm \Delta/2 \\ \mathcal{Z} &= e^{-E^0/T} 2 \cosh(\Delta/2T) \\ \frac{N^+ - N^-}{N} &= \tanh(\Delta/2T), \end{aligned}$$

and the free energy is then given by

$$\begin{aligned} \mathcal{F} &= -T \ln(\mathcal{Z}) = E^0 - T \ln[2 \cosh(\Delta/2T)] \\ &\approx E^0 - T \ln(2) - T \ln \left[ 1 + \frac{\Delta^2}{8T^2} \right] \\ &\approx E^0 - T \ln(2) - \frac{\Delta^2}{8T}. \end{aligned} \quad (26)$$

The magnetization and susceptibility are then determined as

$$m = -\frac{\partial \mathcal{F}}{\partial H} = \frac{\Delta}{4T} \frac{\partial \Delta}{\partial H} \quad (27)$$

$$\chi = \frac{1}{4T} \left( \frac{\partial \Delta}{\partial H} \right)^2 \quad (28)$$

For  $H \rightarrow 0$ , the magnetization  $m$  vanishes and  $\chi$  obeys a Curie law. In order to obtain a Curie-Weiss law, the polarons would have to interact, e.g. via an exchange interaction, or overlap.

- 
- [1] Khomskii, D. I. & Sawatzky, G. A. Interplay between spin, charge and orbital degrees of freedom in magnetic oxides. *Solid State Commun.* **102**, 87–99 (1997).
- [2] Ziese, M. & Thornton, M. J. (eds) *Spin electronics* (Springer, Berlin and Heidelberg, 2001). URL <https://link.springer.com/book/10.1007/3-540-45258-3>.
- [3] Dagotto, E. Complexity in strongly correlated electronic systems. *Science* **309**, 257–262 (2005).
- [4] Emery, V. J., Kivelson, S. A. & Lin, H. Q. Phase separation in the  $t$ - $J$  model. *Phys. Rev. Lett.* **64**, 475–478 (1990).
- [5] Keimer, B., Kivelson, S. A., Norman, M. R., Uchida, S. & Zaanen, J. From quantum matter to high-temperature superconductivity in copper oxides. *Nature* **518**, 179–186 (2015).
- [6] Coey, J. M. D., Viret, M. & von Molnár, S. Mixed-valence manganites. *Adv. Phys.* **48**, 167–293 (1999).
- [7] Kasuya, T. & Yanase, A. Anomalous transport phenomena in Eu-chalcogenide alloys. *Rev. Mod. Phys.* **40**, 684–696 (1968).
- [8] Dietl, T., Śliwa, C., Bauer, G. & Pascher, H. Mechanisms of exchange interactions between carriers and Mn or Eu spins in lead chalcogenides. *Phys. Rev. B* **49**, 2230(R) (1994).
- [9] von Molnár, S. & Stampe, P. A. in *Magnetic polarons* (eds. Kronmüller, H. & Parkin, S.) *Handbook of Magnetism and Advanced Magnetic Materials*, Vol. 5, 2689–2702 (John Wiley & Sons, Ltd., 2007).
- [10] Yakovlev, D. R. & Ossau, W. in *Magnetic polarons* (eds. Kossut, J. & Gaj, J. A.) *Introduction to the Physics of Diluted Magnetic Semiconductors*, Vol. 144 of *Springer Series in Materials Science* 221–262 (Springer, Berlin and Heidelberg, 2010). URL <https://link.springer.com/book/10.1007/978-3-642-15856-8>.
- [11] Wolf, S. A. *et al.* Spintronics: A spin-based electronics vision for the future. *Science* **294**, 1488–1495 (2001).
- [12] Žutić, I., Fabian, J. & Das Sarma, S. Spintronics: Fundamentals and applications. *Rev. Mod. Phys.* **76**, 323–410 (2004).
- [13] Zintl, E. Intermetallische Verbindungen. *Angew. Chem.* **52**, 1–6 (1939).
- [14] Rosa, P. F. S. *et al.* Colossal magnetoresistance in a nonsymmorphic antiferromagnetic insulator. *npj Quantum Mater.* **5**, 52 (2020).
- [15] Ale Crivillero, M. V. *et al.* Surface and electronic structure at atomic length scales of the nonsymmorphic antiferromagnet  $\text{Eu}_5\text{In}_2\text{Sb}_6$ . *Phys. Rev. B* **106**, 035124 (2022).
- [16] Ale Crivillero, M. V. *et al.* Magnetic and electronic properties unveil polaron formation in  $\text{Eu}_5\text{In}_2\text{Sb}_6$ . *Sci. Rep.* **13**, 1597 (2023).
- [17] Park, S. M., Choi, E. S., Kang, W. & Kim, S. J.  $\text{Eu}_5\text{In}_2\text{Sb}_6$ ,  $\text{Eu}_5\text{In}_{2-x}\text{Zn}_x\text{Sb}_6$ : rare earth Zintl phases with narrow band gaps. *J. Mater. Chem.* **12**, 1839–1843 (2002).
- [18] Subbarao, U., Sarkar, S., Joseph, B. & Peter, S. C. Magnetic and x-ray absorption studies on the  $\text{RE}_5\text{X}_2\text{Sb}_6$  (RE = Eu, Yb; X = Al, Ga, In) compounds. *J. Alloys Comp.* **658**, 395–401 (2016).
- [19] Cordier, G. & Stelter, M.  $\text{Sr}_5\text{Al}_2\text{Sb}_6$  and  $\text{Ba}_5\text{In}_2\text{Sb}_6$ : Two new Zintl phases with different chain anions. *Z. Naturforsch. B* **43**, 463–466 (1988).
- [20] Parameswaran, S. A., Turner, A. M., Arovas, D. P. & Vishwanath, A. Topological order and absence of band insulators at integer filling in non-symmorphic crystals. *Nat. Phys.* **9**, 299–303 (2013).
- [21] Wieder, B. J. *et al.* Wallpaper fermions and the nonsymmorphic Dirac insulator. *Science* **361**, 246–251 (2018).
- [22] Morano, V. C. *et al.* Non-collinear 2k antiferromagnetism in the Zintl semiconductor  $\text{Eu}_5\text{In}_2\text{Sb}_6$ . *Phys. Rev. B* **109**, 014432 (2024).
- [23] Rahn, M. C. *et al.* Magnetism in the axion insulator candidate  $\text{Eu}_5\text{In}_2\text{Sb}_6$ . *Phys. Rev. B* **109**, 174404 (2024).
- [24] Mukherjee, G. D., Bansal, C. & Chatterjee, A. Thermal expansion study of ordered and disordered  $\text{Fe}_3\text{Al}$ : An effective approach for the determination of vibrational entropy. *Phys. Rev. Lett.* **76**, 1876–1879 (1996).
- [25] Lindbaum, A. & Rotter, M. in *Spontaneous magnetoelastic effects striction in Gd compounds* (ed. Buschow, K. H. J.) *Handbook of Magnetic Materials*, Vol. 14, 307–362 (Elsevier Science B.V., 2002).
- [26] Ghosh, S. *et al.* Colossal piezoresistance in narrow-gap  $\text{Eu}_5\text{In}_2\text{Sb}_6$ . *Phys. Rev. B* **106**, 045110 (2022).
- [27] Souza, J. C. *et al.* Microscopic probe of magnetic polarons in antiferromagnetic  $\text{Eu}_5\text{In}_2\text{Sb}_6$ . *Phys. Rev. B* **105**, 035135 (2022).
- [28] Teresa, J. M. D. *et al.* Evidence for magnetic polarons in the magnetoresistive perovskites. *Nature* **386**, 256–259 (1997).
- [29] Manna, R. S. *et al.* Lattice strain accompanying the colossal magnetoresistance effect in  $\text{EuB}_6$ . *Phys. Rev. Lett.* **113**, 067202 (2014).
- [30] Franchini, C., Reticcioli, M., Setvin, M. & Diebold, U. Polarons in materials. *Nat. Rev. Mater.* **6**, 560–586 (2021).
- [31] Doerr, M., Rotter, M. & Lindbaum, A. Magnetostriction in rare-earth based antiferromagnets. *Adv. Phys.* **54**, 1–66 (2005).
- [32] Janak, J. F. & Williams, A. R. Giant internal magnetic pressure and compressibility anomalies. *Phys. Rev. B* **14**, 4199–4203 (1976).
- [33] Betancourth, D. *et al.* Magnetostriction reveals orthorhombic distortion in tetragonal Gd compounds. *Phys. Rev. B* **99**, 134406 (2019).
- [34] Sander, D. in *Magnetostriction and magnetoelasticity* (eds. Coey, J. M. D. & Parkin, S. S. P.) *Handbook of Magnetism and Magnetic Materials*, 549–593 (Springer, 2021).
- [35] von Molnár, S. Magnetotransport in magnetic semiconductors and possible applications. *Sensors and Actuators A: Physical* **91**, 161–165 (2001).
- [36] Kaminski, A. & Das Sarma, S. Polaron percolation in diluted magnetic semiconductors. *Phys. Rev. Lett.* **88**, 247202 (2002).
- [37] Das, P. *et al.* Magnetically driven electronic phase separation in the semimetallic ferromagnet  $\text{EuB}_6$ . *Phys. Rev. B* **86**, 184425 (2012).
- [38] Pohlitz, M. *et al.* Evidence for ferromagnetic clusters in the colossal-magnetoresistance material  $\text{EuB}_6$ . *Phys.*

- Rev. Lett.* **120**, 257201 (2018).
- [39] Umehara, M. Effect of the electron-phonon interaction on the self-trapped magnetic polaron. *J. Phys. Soc. Jpn.* **50**, 1082–1090 (1981).
- [40] Kasuya, T. Giant magnetoresistance in  $f$ -electron systems. *J. Appl. Phys.* **77**, 3200–3208 (1995).
- [41] Meskine, H., Saha-Dasgupta, T. & Satpathy, S. Does the self-trapped magnetic polaron exist in electron-doped manganites? *Phys. Rev. Lett.* **92**, 056401 (2004).
- [42] Yu, U. & Min, B. I. Magnetic and transport properties of the magnetic polaron: Application to  $\text{Eu}_{1-x}\text{La}_x\text{B}_6$  system. *Phys. Rev. Lett.* **94**, 117202 (2005).
- [43] Kagan, M. Y., Kugel, K. I., Rakhmanov, A. L. & Pазhitnykh, K. S. Small-scale phase separation in doped anisotropic antiferromagnets. *J. Phys.: Condens. Matter* **18**, 10905–10914 (2006).
- [44] Jung, M.-H. *et al.* Anisotropic transport and magnetic properties and magnetic-polaron-like behavior in  $\text{CeTe}_{2-x}$ . *J. Phys. Soc. Jpn.* **69**, 937–944 (2000).
- [45] Shon, W., Rhyee, J.-S., Jin, Y. & Kim, S.-J. Magnetic polaron and unconventional magnetotransport properties of the single-crystalline compound  $\text{EuBiTe}_3$ . *Phys. Rev. B* **100**, 024433 (2019).
- [46] Song, Y., Shi, N., Deng, S., Xing, X. & Chen, J. Negative thermal expansion in magnetic materials. *Prog. Mater. Sci.* **121**, 100835 (2021).
- [47] He, J.-C. *et al.* Magnetic-field-induced sign changes of thermal expansion in  $\text{DyCrO}_4$ . *Chin. Phys. Lett.* **40**, 066501 (2023).
- [48] Hemberger, J., Krug von Nidda, H.-A., Tsurkan, V. & Loidl, A. Large magnetostriction and negative thermal expansion in the frustrated antiferromagnet  $\text{ZnCr}_2\text{Se}_4$ . *Phys. Rev. Lett.* **98**, 147203 (2007).
- [49] Li, B. *et al.* Colossal negative thermal expansion induced by magnetic phase competition on frustrated lattices in laves phase compound  $(\text{Hf,Ta})\text{Fe}_2$ . *Phys. Rev. B* **93**, 224405 (2016).
- [50] Rao, C. N. R. & Cheetham, A. K. Giant magnetoresistance in transition metal oxides. *Science* **272**, 369–370 (1996).
- [51] Inoue, J. in *GMR, TMR and BMR* (ed. Shinjo, T.) *Nanomagnetism and Spintronics* Ch. 2, 15–92 (Elsevier, Amsterdam, 2009).
- [52] Laue-Camera GmbH (2024). Dr. Andreas Erb, <https://www.lauecamera.com>.
- [53] KÜchler, R., Bauer, T., Brando, M. & Steglich, F. A compact and miniaturized high resolution capacitance dilatometer for measuring thermal expansion and magnetostriction. *Rev. Sci. Instrum.* **83**, 095102 (2012).
- [54] Quantum Design Inc. (2023). <https://www.qdusa.com>.
- [55] KÜchler, R., Wawrzyńczak, R., Dawczak-Dębicki, H., Gooth, J. & Galeski, S. New applications for the world’s smallest high-precision capacitance dilatometer and its stress-implementing counterpart. *Rev. Sci. Instrum.* **94**, 045108 (2023).
- [56] Mukherjee, G. D., Chatterjee, A. & Bansal, C. Anomalous thermal expansion behavior of the  $\text{YBaCuO}$  superconductor. Indirect evidence of polaron formation. *Physica C* **232**, 241–245 (1994).
- [57] Schmiedeshoff, G. M. *et al.* Versatile and compact capacitive dilatometer. *Rev. Sci. Instrum.* **77**, 123907 (2006).
- [58] Emin, D. & Hillery, M. S. Continuum studies of magnetic polarons and bipolarons in antiferromagnets. *Phys. Rev. B* **37**, 4060–4070 (1988).

## Acknowledgements

S.W. acknowledges fruitful discussion with Oliver Stockert. Work at the Max-Planck-Institute for Chemical Physics of Solids in Dresden and at Goethe University Frankfurt was supported by the Deutsche Forschungsgemeinschaft (DFG, German Research Foundation), Project No. 449866704. Work at Los Alamos was performed under the auspices of the U.S. Department of Energy, Office of Basic Energy Sciences, Division of Materials Science and Engineering. M.S.C. acknowledges support from the Los Alamos Laboratory Directed Research and Development Program.

## Author contributions

S.W. and J.M. conceived the experiments, M.S.C. and P.F.S.R. prepared the samples, H.D.-D., M.V.A.C. and S.M.T. conducted the experiments, U.K.R. and P.S. provided theoretical insight, M.V.A.C. and S.W. analysed the results, S.W. and P.S. wrote the draft, with help from M.V.A.C., J.M. and U.K.R. All authors contributed to the discussion of the results and the revision of the manuscript.

## Competing interests

The authors declare no competing interests.